Diagnosing Current Distributions in Batteries with Magnetic Resonance Imaging

Mohaddese Mohammadi^{a\$}, Emilia V. Silletta^{a\$}, Andrew J. Ilott ^a, Alexej Jerschow*^a

^a Department of Chemistry, New York University, 100 Washington Square East, New York, New York, 10003, USA.

^{*}Corresponding Author: alexej.jerschow@nyu.edu

[§] These authors contributed equally to the work.

Abstract

Batteries and their defects are notoriously difficult to analyze non-destructively, and consequently, many defects and failures remain little noticed and characterized until they cause grave damage. The measurement of the current density distributions inside a battery could reveal information about ideal cell behavior and its deviations from it, and could thus provide early signs of deterioration or failures. Here, we describe methodology for fast nondestructive assessment and visualization of the effects of current distributions inside Li-ion pouch cells. The technique, based on magnetic resonance imaging (MRI), allows measuring the magnetic field maps during charging/discharging. Marked changes in the distributions are observed as a function of the state of charge, and also upon sustaining damage. In particular, it is shown that the current distribution is non-linear with overall charge/discharge current, is generally asymmetric with respect to switching the sign of the current, and a qualitative symmetry between full charge and full discharge is observed. This technique could potentially be of great utility in diagnosing the health of cells and their behavior under different charging or environmental conditions.

Keywords

Rechargeable Li-ion batteries, Current distribution, Magnetic Resonance Imaging

INTRODUCTION

Nondestructive battery cell testing is of critical importance in employing rechargeable batteries in portable devices, transportation, and in energy storage grids. The accurate prediction of cell and battery lifetime and their capacity fading is of intense interest in many parts of a battery's deployment cycle. There is a lack of fast nondestructive techniques that can provide detailed and localized diagnostic data for fully assembled cells. Here, we describe a Magnetic Resonance Imaging (MRI) based technique that can provide an assessment of current distributions within cells quickly, and is also compatible with many commercial cell designs.

The current distribution within cells is affected by the design and resistance profile of each part of the cell, the heterogeneity of the electrodes, and the type and location of any physical defects such as dendrites or pre-existing cracks¹. Non-uniform current distributions can be the source of cell failures or capacity loss, often initiated and accompanied by lithium dendrite growth, or assembly imperfections. For example, it was shown that there was a direct correlation between energy density and the non-uniformity of the current distribution, demonstrating a potential to gain as much as 50% in energy density through improving the current distribution². Prior work on measuring current distributions include studies with cell hardware modifications. For example, the implementation of tabs in different positions along the electrodes provided a means of inferring the variability of current^{3,4}, which demonstrated the significant changes evident in the current, depending on the charge/discharge rate. It is therefore of great interest to perform *in situ* or *operando*, non-invasive, and spatially-resolved measurements of current distributions, as it can pave the way for developing safer and higher performance batteries.

Nuclear magnetic resonance (NMR) and magnetic resonance imaging (MRI) techniques have established themselves as tools for in situ and operando studies of fundamental cell mechanisms including studies of failure modes, charge storage mechanisms, and ion mobility^{5–8}. Stray field NMR studies have been used to map lithium in electrodes⁹. Electron paramagnetic resonance in situ / operando methodology has been demonstrated for mapping metallic lithium and dendrites^{10–12}. Other in situ / operando methodology include synchrotron-based scanning transmission X-ray microscopy (STXM)¹³ and X-ray micro-diffraction¹⁴, energy dispersive X-ray diffraction (EDXRD) ¹⁵, X-ray diffraction in combination with other spectroscopic methods such as transmission electron microscopy (TEM)^{16,17}, operando neutron diffraction,¹⁸ operando video microscopy¹⁹, and Raman spectroscopy²⁰. All these techniques typically require the fabrication of special cells for the study of cell processes.

There are fewer choices of techniques for measuring unaltered commercial-type cells, which have opaque and typically conductive enclosures. Consequently, the amount of information obtainable from such measurements is significantly limited. Notable exceptions include, for example, a fast acoustic method^{21,22}, electrical measurements²³, and X-ray computed tomography (CT)²⁴.

In previous work, we have introduced an MRI technique to assess state-of-charge (SOC) via the magnetic fields induced by the magnetic susceptibility of the active cell components, which was based on sensing the induced magnetic field changes of the active materials in the cell⁶. This approach provided fast, nondestructive mapping of SOC and defects. Since the method does not require access to the inside of the cell, it will henceforth be termed inside-out MRI (abbreviated as ioMRI). This ioMRI method is shown here to be suitable for the diagnostics of current distributions within cells as well. A fundamental limitation of applying this method to commercial lithium-ion cells is poor radiofrequency (rf) penetration due to the conductive casing and the electrodes^{25,5,26}. The ioMRI technique, however, avoids this complication by simply measuring fields around the device, not within it.

Magnetic fields have been measured for assessing currents before, such as, for example using magneto-optic imaging for studying the flux and current distribution of a long thin strip²⁷. MRI-based current imaging was first described by Manassen et al.²⁸, and this type of methodology is currently being applied *in vivo* for the purpose of electrical property mapping^{29–34}. It was also suggested, for example, that neuronal current distributions could be imaged using magnetic resonance imaging^{35,31}.

In this article, we demonstrate a technique for assessing current distributions within commercial-type Li-ion pouch cells. Experiments were performed with different discharging/charging current rates on healthy and mechanically stressed cells. Marked differences were observed as a function of state of charge (SOC) and after stressing the cell. It is also demonstrated that the current distribution is significantly asymmetric when switching from charge to discharge current, the current distribution is nonlinear with respect to overall applied current, and there is an interesting symmetry between states at full charge and near full discharge.

EXPERIMENTAL

Cells: Stacked electrode Li-ion pouch cells were used for imaging. Multilayer stacked electrode cells were manufactured as described previously⁶ at the battery prototyping center at Rochester Institute of Technology (RIT)with a capacity of 250 mAh and a nominal voltage of 3.7 V. The material that were used for the cell construction were Li_{1.02}Ni_{0.50}Mn_{0.29}Co_{0.19}O₂ as the cathode, Graphite as the anode and 1.2 M LiPF₆ EC:DMC 3:7 as the electrolyte. For increasing the conductivity and structure of working electrodes Powder grade carbon black and PVDF were used.

Battery holders: Cylindrical holders with 39-mm diameter were designed in Tinkercad and 3D printed with a Polylactic Acid (PLA) filament. The holders were filled with a 15 mM $CuSO_4$ solution in water, giving a 1H T_1 relaxation constant of 100ms.

Cycling conditions: In order to fully charge cells (up to voltage 4.2V), cells were first charged with a current of 25mA (0.1C). Then, for each step of SOC, RIT cells were discharged with 125mA (0.5C) until the cell reached 2.5V. Cells were always operated between 4.2V and 2.5V. During current imaging, the cell was charging and discharging with a constant current protocol using a Biologic VSP potentiostat. The cycler remained connected to the cell throughout all measurements. An aluminum foil and an in-line low-pass filter with cutoff frequency of 1.9 MHz were used to shield the probe area from rf interference.

Magnetic Resonance Imaging: A 9.4T Bruker Ultrashield Avance I spectrometer with a Bruker mini0.75 gradient assembly was used for performing the MRI experiments. The resonance frequency of ¹H in the spectrometer was 400.1 MHz. For imaging and data collection, a Bruker MiniWB57 imaging probe was used with a Bruker WB57 40-mm i.d. coil insert for ¹H experiments.

A slice selective 2D fast low angle shot (FLASH) sequence with nominal flip angle (α) of 15°, TR of 100 ms, 12 scans of averaging, and four different echo times of 2.45, 2.5, 2.75, and 2.80ms were used to acquire the 2D 1 H images. The readout direction was along z while x was the phase-encoded dimension and 128 points were collected along each dimension. The field of view (FOV) was 51.2mm in the x and z-direction, which resulted in a 400 μ m resolution. The slice thickness was 1mm. Each 2D experiment took approximately 2.5min.

Calculations: Finite Element calculations were performed with COMSOL Multiphysics with the AC/DC module. A stacked-electrode cell and one jelly-rolled cell model were created in COMSOL (a calculation for a jelly-rolled cell yielded similar results). The calculation utilized the AC/DC module and solved Ampere's Law with current conservation boundary conditions.

The model of the stacked-cut electrode battery was composed of two single-sided coated anodes, one double-sided coated cathode, two aluminum current collectors, one copper current collector and three tabs for positive and negative ports. A mesh of 11,930,062 elements was used for finite element analysis. In the simulation of the charging/discharging condition, the copper tab of the battery was assigned as the positive/negative constant current terminal and the aluminum tabs were always grounded. Supplementary Figure S2 shows a depiction of the model.

The phase map was calculated from phase images using an unwrapping algorithm as described previously.⁶

RESULTS AND DISCUSSION

Cells were placed in an a slot in a custom-designed holder, containing compartments for water, as described previously⁶. For the measurements reported here a 15mM CuSO4 water solution was used as the detection medium in order to shorten the T_1 relaxation time constant and thus allow faster imaging. The arrangement used is illustrated in Figure 1A. The MRI signals were obtained from the water compartment and all represented images in this article originated from a slice midway across the cell as indicated in Figure. 1A. The measurement was based on a slice-selective FLASH imaging sequence, with different echo times. The different echo times allowed encoding the precession angles, from which the local precession frequency could be obtained accurately. After phase unwrapping, magnetic field images were produced. Only currents perpendicular to the static magnetic field led to observable fields, as the spin precession is only significantly affected by magnetic field components collinear with B_0 . The orientations of the different coordinate axes are indicated in Figure 1B.

Figure 1C shows the results from a current distribution calculation, considering an ideal rectangular electrode assembly (as shown in Figure S2) and negligible effects from non-uniform charge states. The current pattern for both the positive and negative electrodes looks the same in this calculation, except that the polarity is reversed. The current distribution resembles those previously determined by theoretical and computational means³⁶.

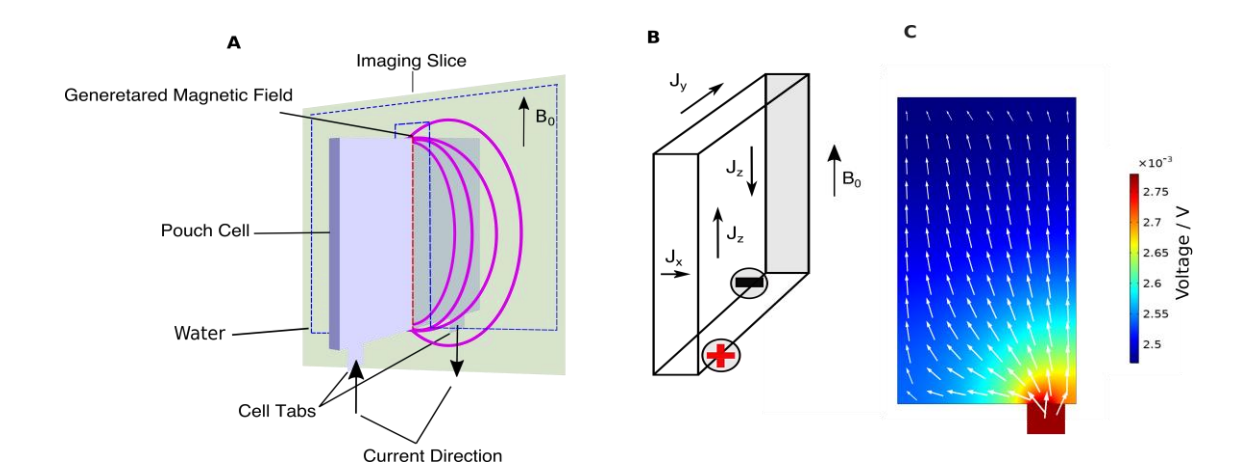


Figure 1. Illustration of the experimental arrangement and measured quantities. (A) Cell position and orientation of imaging slice, as well as indication of the detected volume (dashed rectangle). (B) Current distribution elements inside the battery and cell orientation. (C) Calculated current and voltage distribution on the positive current collector during charging.

To explore the effect of the SOC on the current distribution, a cell made with 5 stacked double-coated cathode/anode layers, was first fully charged to 4.2 V, and then measured after discharging it by the specific amounts shown in Figure 2. The measurements were performed while either discharge or charge current was applied around the indicated depth of discharge (DOD). From each obtained field map, a resting-state reference image at the same DOD was subtracted. This process was essential, because at the magnetic field used (9.4 T), the susceptibility effect was much stronger than the effect produced by the current (in Figure S1, the effect of susceptibility at different SOC is shown). It is seen that a significant change in the current-produced magnetic fields is observed at the different DOD for both charge and discharge current.

Generally, the highest fields observed are near the tab, which is expected. As the DOD increases, maxima develop in other locations, in particular also at the opposite end (top of the cell). This aspect is particularly interesting, as this phenomenon is related to a nonuniformity in SOC across the cathode. Figure S1, in particular, shows the field maps during the resting period (without current flow) for comparison. As described previously, these images can be interpreted as showing mostly a distribution of the SOC across the cathode (for this battery material).⁶ As the cathode material is enriched with lithium more and more, the magnetic susceptibility increases and the effect on the magnetic field increases as well. It is seen that 'hot spots' shown in Figure 2

also appear as spots of maxima in Figure S1, thus indicating that current flow is correlated with areas of highest susceptibility and thus areas of highest DOD.

It is of note that there is no symmetry between maps for charge and discharge current at the same DOD, i.e. current is not simply reversed. This is expected, of course, because, for example, at low DOD (near full charge), there is only a small fraction of active material that is able to accept the charge, and it is much more dispersed, while during the discharge operation, current can be drawn from most charged areas. A similarly large asymmetry is observed for the highest DOD case: in this situation, during discharge, there are few areas that can produce current easily from the stored charge, while there are many more areas that can accept current during charging.

The two extreme cases, high and low DOD, however, observe an interesting symmetry when considered together. In the magnetic field histograms (Figure 2) for the lowest DOD, one can see only one single peak in the negative range for the field from discharge current and two peaks (positive/negative) for charge current. For the highest DOD, the situation is reversed: a single peak is observed in the positive field range for charge current and two peaks for discharge current. The flip in sign for overall current is relatively straightforward to understand – the direction of the current is reversed. With regard to the difference between a single peak or a double peak, one can provide the following explanation: Considering that a more or less uniform current is flowing along the *y*-direction, one would expect the magnetic field to be positive on one side of the cell and negative on the other, which would generate a double-peaked distribution. At low DOD, during charging, current is only weakly perturbed by the influence of active material, because the majority of the material is saturated. A similar situation is encountered for high DOD during discharge current – little active material is available to provide strong non-uniform perturbations in the current. Hence, in these two situations, one would expect a double-peaked distribution, centered around zero field, as was indeed observed.

A simulation was performed in order to explore this last point: the calculation was performed in a cell model while neglecting the contribution of active material. The model for this calculation is shown in Figure S2. The result is shown in the bottom right panel of Figure 2. The calculation shows the clear emergence of a double peak. The magnetic field range predicted is also in the same numerical range as shown in the experiments. The inner sharp peaks arise from areas further away from the cell, which may not be included in the experiment. Furthermore, the histogram also shows significant areas of very high positive and negative fields. These areas correspond to regions that are very close to the cell and may result in signal cancellation due to partial volume

effects, and would thus not be observable in the experiment. Further minor differences may be due to the fact that the simulation did not incorporate any SOC inhomogeneities. Overall, there is hence a good conceptual agreement between this model calculation and the experiments in the regimes described above (at maximum and minimum DOD).

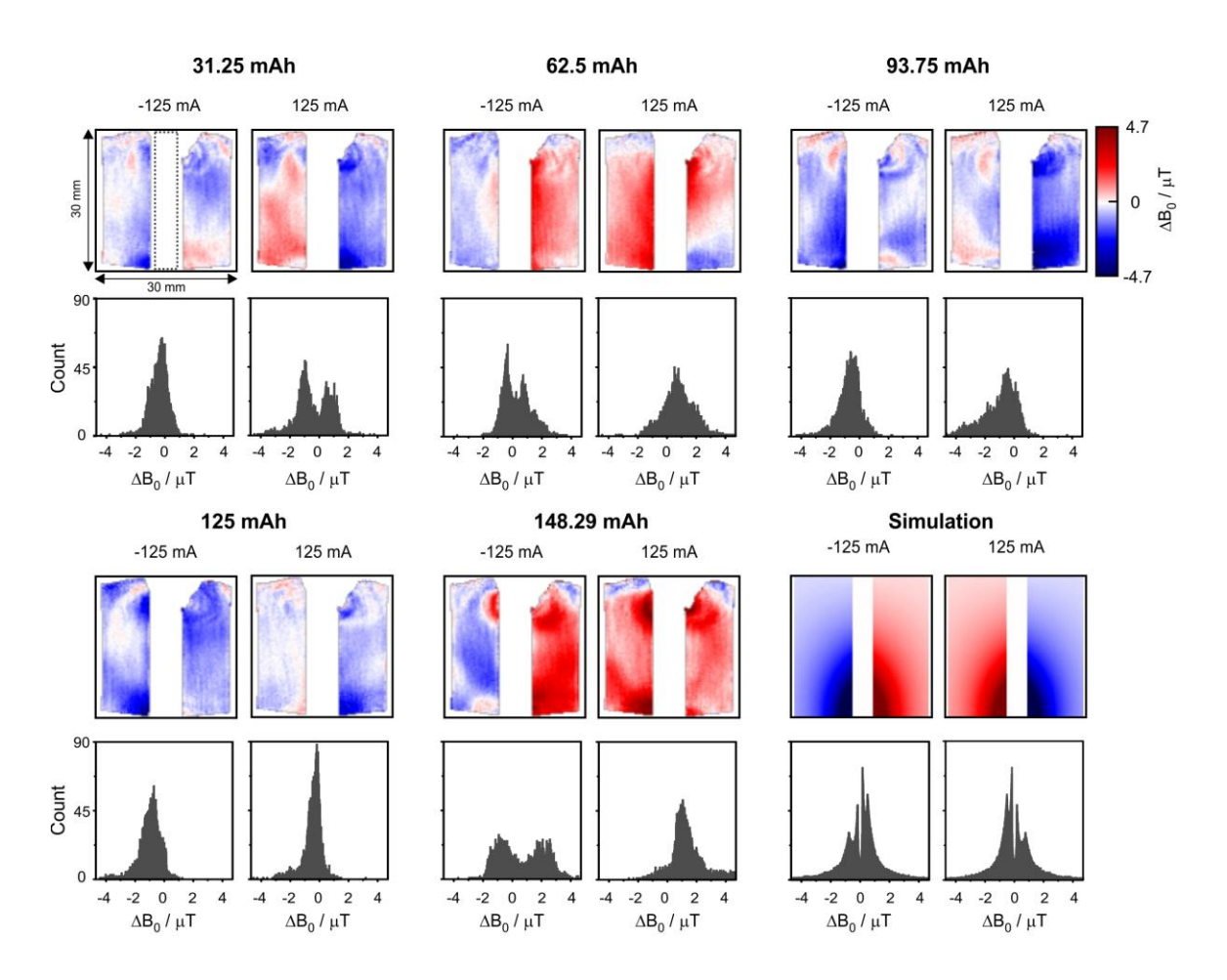


Figure 2. Magnetic field maps and histograms during discharge (negative current) and charge (positive current) at different depth of discharge (DOD) as indicated. The bottom right panel shows a simulation. The battery leads in these measurements are located at the bottom of each map. The discharge capacity is indicative of the starting point of each step, and discharge measurements were performed before charge measurements. The imaging dimensions and the location of the cell (dotted rectangle) are indicated in the top left image.

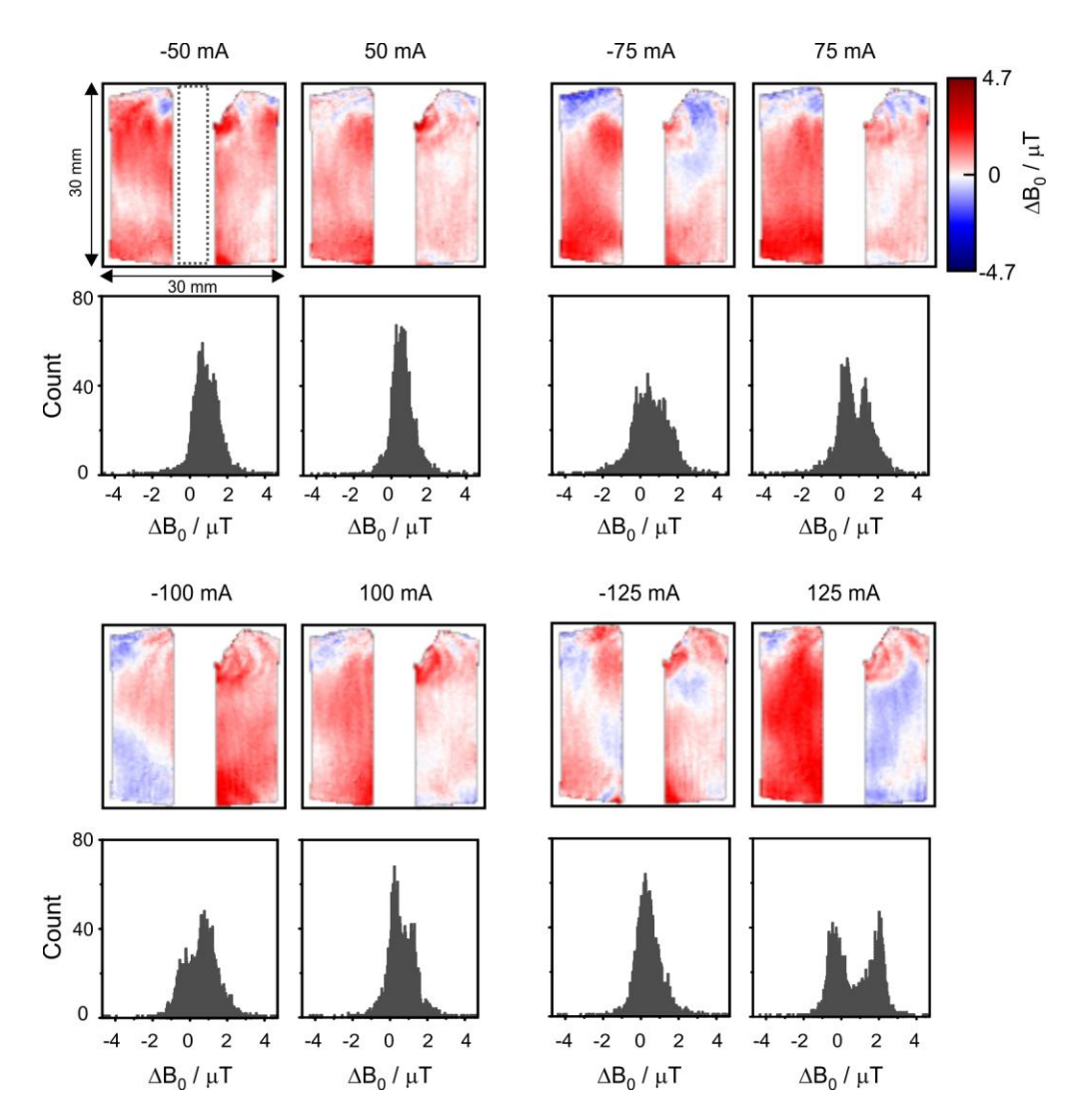


Figure 3. Magnetic field maps and histograms as a function of overall discharge/charge current near full charge (DOD = 0 mAh). The imaging dimensions and the location of the cell (dotted rectangle) are indicated in the top left image.

In order to investigate the effect of current further, experiments were performed at full SOC (i.e. DOD=0 mAh) with different overall currents used for discharge and charge operation. The histogram clearly shows that the double-peak pattern develops only above a certain threshold current (75 mA), is strongest at 125 mA, and remains absent for negative current (discharging), which is in line with the discussion in relation to Figure 2. This effect could be rationalized by considering that a smaller current is affected more by perturbations from the active material.

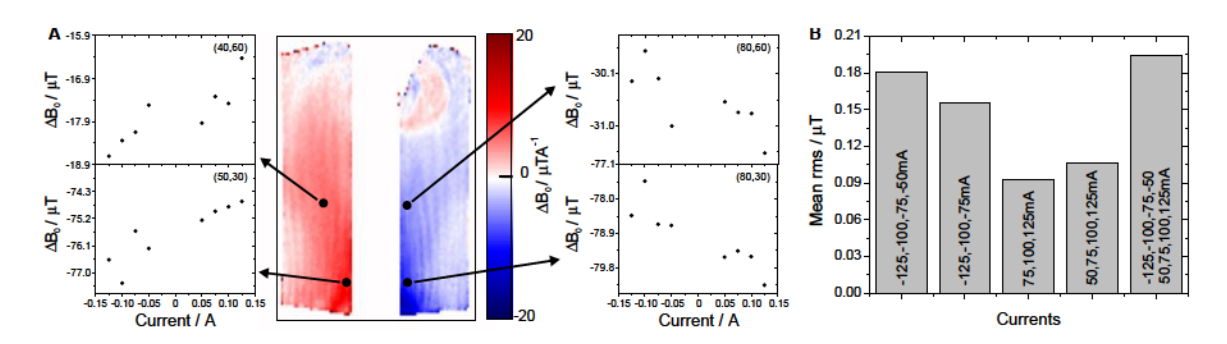


Figure 4. (A) In the center, the spatially resolved map shows the result of a linear per-voxel fit of magnetic field vs. current, using all the current regimes measured (-125, -100, -75, -50, 50, 75, 100, 125mA). Several points are extracted for illustration, showing the magnetic field vs. current at each location. (B) Root mean square deviation of the linear fits across the whole volume performed by using different data combinations as indicated.

In order to further examine the regimes of linearity of field vs. applied current, an analysis was performed to fit a linear model on a voxel-by-voxel basis to the magnetic field produced as a function of overall applied current. Figure 4A shows the results for the slope (field per unit current) if the maps obtained for all currents (positive and negative) are used for the fit. Examination of this map indicated that there were marked non-linearities in many data points as demonstrated in the selection shown in Figure 4A. These illustrate a significant deviation from linearity, especially in the negative current regime. In order to provide a quantitative test for overall linearity, different combinations of maps were used for the fit, and the average root-meansquare deviation in the linear fit for each pixel was calculated across the whole measurement volume (Figure 4B). It is seen clearly that the deviation from linear behavior is largest if data from all measured current regimes are used. The largest deviation can be traced to originate from the negative current points (see the first two bars in Figure 4B, which have similarly high rootmeam-square deviation values). The smallest deviation was found when only the three highest current regimes were used, and it was only slightly larger if the 50 mA point was included. This finding highlights the significant deviation from linear behavior for the discharge regime. This result is in line with earlier arguments that near full SOC, the discharge current experiences significant contributions from the active material, whereby the current distribution would be significantly altered. During charge, however, current flows more uniformly, and the active material does not produce significant inhomogeneities in the measurement.

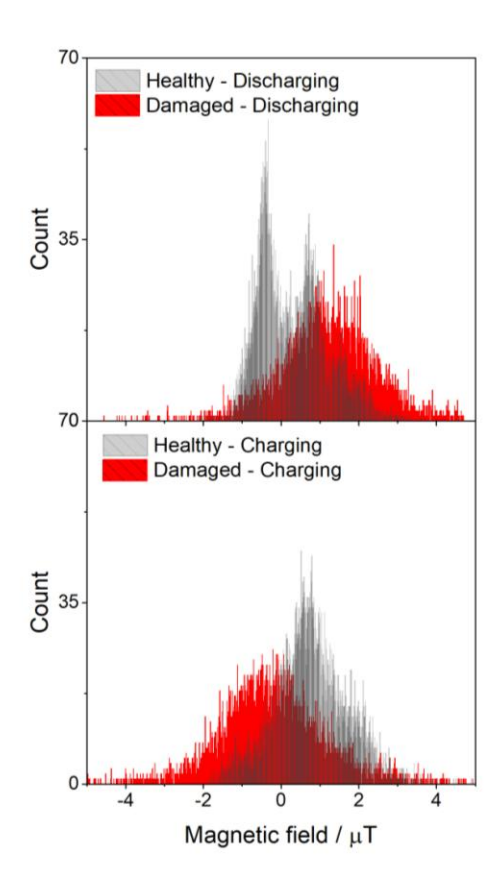


Figure 5. Histograms calculated from the magnetic field maps during discharging and charging for a damaged cell at 62.5 mAh DOD (after subtracting a reference image in the resting state).

Finally, it is demonstrated that the current distribution is significantly altered when a cell is damaged. Figure 5 shows the magnetic field histograms after damaging the cell by dropping a 245 gram rod, with 1 cm diameter from a height of 30 cm, resulting in an energy released per unit area of 9175.79 J/m2. Pictures of the drop-rod system and damaged cell are shown in Figure S3 and Figure S4. The damage led to significant changes in the current distribution, as is clearly observed in Figure 5.

CONCLUSION

In summary, we have demonstrated here an MRI-based technique for the nondestructive assessment of current distributions within rechargeable Li-ion cells. The technique, referred to as an "inside-out" MRI approach (ioMRI), revealed an asymmetry in the current distributions

between charging and discharging, which evolved as a function of SOC. The behavior near full SOC during charge operation and at high DOD during discharge operation demonstrated a notable similarity, which is indicative of less localized and less pronounced perturbations from the active material. Furthermore, it was found that the observed magnetic field distribution was nonlinear w.r.t. overall applied current (for example, it was most linear for charging near full charge and least linear for discharging in this state). Damages to the cell showed marked changes in current distributions as well. This measurement methodology shows promise for quick noninvasive assessment of cell behavior during charging and discharging and for determining the evolution of cell behavior.

Acknowledgements

Funding was provided by grants from the US National Science Foundation under programs CBET 1804723 and PFI-TT 1827585. We acknowledge the support from the Battery Prototyping Center team at the Rochester Institute of Technology (RIT), Dr. Matthew Ganter and Dr. Christopher Schauerman.

Author Contributions

M.M. and E.V.S contributed equally to the work. M.M, A.J. and A.J.I. designed the experiments. M.M. carried out the experiments and simulations. E.V.S performed the calculation and generated images. M.M, E.V.S and A.J. Analyzed the results and wrote the paper.

Declaration of interests

The authors declare no competing interests.

REFERENCES

- 1. D. R. Baker and M. W. Verbrugge, Temperature and Current Distribution in Thin Film Batteries, *J. Electrochem. Soc.*, 1999, **146**, 2413–2424.
- 2. G. Zhang, C. E. Shaffer, C.-Y. Wang and C. D. Rahn, Effects of Non-Uniform Current Distribution on Energy Density of Li-Ion Cells, *J. Electrochem. Soc.*, 2013, **160**, A2299–A2305.
- 3. A. Samba, N. Omar, H. Gualous, O. Capron, P. Van den Bossche and J. Van Mierlo, Impact of Tab Location on Large Format Lithium-Ion Pouch Cell Based on Fully Coupled Tree-Dimensional Electrochemical-Thermal Modeling, *Electrochimica Acta*, 2014, 147, 319–329.
- 4. G. Zhang, C. E. Shaffer, C.-Y. Wang and C. D. Rahn, In-Situ Measurement of Current Distribution in a Li-Ion Cell, *J. Electrochem. Soc.*, 2013, **160**, A610–A615.
- 5. A. J. Ilott, M. Mohammadi, H. J. Chang, C. P. Grey and A. Jerschow, Real-time 3D imaging of microstructure growth in battery cells using indirect MRI, *Proc. Natl. Acad. Sci.*, 2016, **113**, 10779–10784.
- 6. A. J. Ilott, M. Mohammadi, C. M. Schauerman, M. J. Ganter and A. Jerschow, Rechargeable lithium-ion cell state of charge and defect detection by in-situ inside-out magnetic resonance imaging, *Nat. Commun.*, 2018, **9**, 1776.
- 7. A. J. Ilott, N. M. Trease, C. P. Grey and A. Jerschow, Multinuclear *in situ* magnetic resonance imaging of electrochemical double-layer capacitors, *Nat. Commun.*, 2014, 5, 4536.
- 8. H. J. Chang, A. J. Ilott, N. M. Trease, M. Mohammadi, A. Jerschow and C. P. Grey, Correlating Microstructural Lithium Metal Growth with Electrolyte Salt Depletion in Lithium Batteries Using 7Li MRI, *J. Am. Chem. Soc.*, 2015, **137**, 15209–15216.
- 9. J. A. Tang, S. Dugar, G. Zhong, N. S. Dalal, J. P. Zheng, Y. Yang and R. Fu, Non-Destructive Monitoring of Charge-Discharge Cycles on Lithium Ion Batteries using ⁷Li Stray-Field Imaging, *Sci. Rep.*, 2013, **3**, srep02596.
- 10. A. Niemöller, P. Jakes, R.-A. Eichel and J. Granwehr, EPR Imaging of Metallic Lithium and its Application to Dendrite Localisation in Battery Separators, *Sci. Rep.*, , DOI:10.1038/s41598-018-32112-y.
- 11. J. Wandt, C. Marino, H. A. Gasteiger, P. Jakes, R.-A. Eichel and J. Granwehr, Operando electron paramagnetic resonance spectroscopy formation of mossy lithium on lithium anodes during charge–discharge cycling, *Energy Environ. Sci.*, 2015, **8**, 1358–1367.

- 12. M. Sathiya, J.-B. Leriche, E. Salager, D. Gourier, J.-M. Tarascon and H. Vezin, Electron paramagnetic resonance imaging for real-time monitoring of Li-ion batteries, *Nat. Commun.*, 2015, **6**, 6276.
- 13. J. Lim, Y. Li, D. H. Alsem, H. So, S. C. Lee, P. Bai, D. A. Cogswell, X. Liu, N. Jin, Y. Yu, N. J. Salmon, D. A. Shapiro, M. Z. Bazant, T. Tyliszczak and W. C. Chueh, Origin and hysteresis of lithium compositional spatiodynamics within battery primary particles, *Science*, 2016, **353**, 566–571.
- 14. J. Liu, M. Kunz, K. Chen, N. Tamura and T. J. Richardson, Visualization of Charge Distribution in a Lithium Battery Electrode, *J. Phys. Chem. Lett.*, 2010, **1**, 2120–2123.
- 15. W. A. Paxton, Z. Zhong and T. Tsakalakos, Tracking inhomogeneity in high-capacity lithium iron phosphate batteries, *J. Power Sources*, 2015, **275**, 429–434.
- 16. M. Morcrette, Y. Chabre, G. Vaughan, G. Amatucci, J.-B. Leriche, S. Patoux, C. Masquelier and J.-M. Tarascon, In situ X-ray diffraction techniques as a powerful tool to study battery electrode materials, *Electrochimica Acta*, 2002, 47, 3137–3149.
- 17. J.-H. Cheng, A. A. Assegie, C.-J. Huang, M.-H. Lin, A. M. Tripathi, C.-C. Wang, M.-T. Tang, Y.-F. Song, W.-N. Su and B. J. Hwang, Visualization of Lithium Plating and Stripping via in Operando Transmission X-ray Microscopy, *J. Phys. Chem. C*, 2017, **121**, 7761–7766.
- 18. S. Taminato, M. Yonemura, S. Shiotani, T. Kamiyama, S. Torii, M. Nagao, Y. Ishikawa, K. Mori, T. Fukunaga, Y. Onodera, T. Naka, M. Morishima, Y. Ukyo, D. S. Adipranoto, H. Arai, Y. Uchimoto, Z. Ogumi, K. Suzuki, M. Hirayama and R. Kanno, Real-time observations of lithium battery reactions—operando neutron diffraction analysis during practical operation, *Sci. Rep.*, 2016, **6**, 28843.
- 19. K. N. Wood, E. Kazyak, A. F. Chadwick, K.-H. Chen, J.-G. Zhang, K. Thornton and N. P. Dasgupta, Dendrites and Pits: Untangling the Complex Behavior of Lithium Metal Anodes through Operando Video Microscopy, *ACS Cent. Sci.*, 2016, **2**, 790–801.
- 20. J.-C. Panitz, P. Novák and O. Haas, Raman Microscopy Applied to Rechargeable Lithium-Ion Cells-Steps towards in situ Raman Imaging with Increased Optical Efficiency, *Appl. Spectrosc.*, 2001, **55**, 1131–1137.
- 21. A. G. Hsieh, S. Bhadra, B. J. Hertzberg, P. J. Gjeltema, A. Goy, J. W. Fleischer and D. A. Steingart, Electrochemical-acoustic time of flight: in operando correlation of physical dynamics with battery charge and health, *Energy Environ. Sci.*, 2015, **8**, 1569–1577.
- 22. G. Davies, K. W. Knehr, B. V. Tassell, T. Hodson, S. Biswas, A. G. Hsieh and D. A. Steingart, State of Charge and State of Health Estimation Using Electrochemical Acoustic Time of Flight Analysis, *J. Electrochem. Soc.*, 2017, **164**, A2746–A2755.
- 23. R. Petibon, C. P. Aiken, N. N. Sinha, J. C. Burns, H. Ye, C. M. VanElzen, G. Jain, S. Trussler and J. R. Dahn, Study of Electrolyte Additives Using Electrochemical Impedance Spectroscopy on Symmetric Cells, *J. Electrochem. Soc.*, 2013, **160**, A117–A124.
- 24. D. P. Finegan, M. Scheel, J. B. Robinson, B. Tjaden, I. Hunt, T. J. Mason, J. Millichamp, M. Di Michiel, G. J. Offer, G. Hinds, D. J. L. Brett and P. R. Shearing, *In-operando* high-speed tomography of lithium-ion batteries during thermal runaway, *Nat. Commun.*, 2015, **6**, 6924.

- 25. A. J. Ilott, S. Chandrashekar, A. Klöckner, H. J. Chang, N. M. Trease, C. P. Grey, L. Greengard and A. Jerschow, Visualizing skin effects in conductors with MRI: 7Li MRI experiments and calculations, *J. Magn. Reson.*, 2014, **245**, 143–149.
- 26. A. J. Ilott and A. Jerschow, Super-resolution Surface Microscopy of Conductors using Magnetic Resonance, *Sci. Rep.*, 2017, 7, 5425.
- 27. TH. Johansen, M. Baziljevich, H. Bratsberg, Y. Galperin, PE. Lindelof, Y. Shen and P. Vase, Direct observation of the current distribution in thin superconducting strips using magneto-optic imaging, *Phys. Rev. B Condens. Matter*, 1996, **54**, 16264–16269.
- 28. Y. Manassen, E. Shalev and G. Navon, Mapping of electrical circuits using chemical-shift imaging, *J. Magn. Reson.* 1969, 1988, **76**, 371–374.
- 29. M. Joy, G. Scott and M. Henkelman, In vivo detection of applied electric currents by magnetic resonance imaging, *Magn. Reson. Imaging*, 1989, 7, 89–94.
- 30. D. S. Tuch, V. J. Wedeen, A. M. Dale, J. S. George and J. W. Belliveau, Conductivity tensor mapping of the human brain using diffusion tensor MRI, *Proc. Natl. Acad. Sci.*, 2001, **98**, 11697–11701.
- 31. M. L. G. Joy, V. P. Lebedev and J. S. Gati, Imaging of current density and current pathways in rabbit brain during transcranial electrostimulation, *IEEE Trans. Biomed. Eng.*, 1999, **46**, 1139–1149.
- 32. X. Zhang, S. Zhu and B. He, Imaging Electric Properties of Biological Tissues by RF Field Mapping in MRI, *IEEE Trans. Med. Imaging*, 2010, **29**, 474–481.
- 33. A. L. H. M. W. van Lier, D. O. Brunner, K. P. Pruessmann, D. W. J. Klomp, P. R. Luijten, J. J. W. Lagendijk and C. A. T. van den Berg, B Phase mapping at 7 T and its application for in vivo electrical conductivity mapping, *Magn. Reson. Med.*, 2012, **67**, 552–561.
- 34. J. Shin, M. J. Kim, J. Lee, Y. Nam, M. Kim, N. Choi, S. Kim and D.-H. Kim, Initial study on in vivo conductivity mapping of breast cancer using MRI, *J. Magn. Reson. Imaging*, 2015, **42**, 371–378.
- 35. N. W. Halpern-Manners, V. S. Bajaj, T. Z. Teisseyre and A. Pines, Magnetic resonance imaging of oscillating electrical currents, *Proc. Natl. Acad. Sci.*, 2010, **107**, 8519–8524.
- 36. P. Taheri, A. Mansouri, M. Yazdanpour and M. Bahrami, Theoretical Analysis of Potential and Current Distributions in Planar Electrodes of Lithium-ion Batteries, *Electrochimica Acta*, 2014, **133**, 197–208.

Figure Legends

Figure 1. Illustration of the experimental arrangement and measured quantities. (A) Cell position and orientation of imaging slice, as well as indication of the detected volume (dashed rectangle). (B) Current distribution elements inside the battery and cell orientation. (C) Calculated current and voltage distribution on the positive current collector during charging.

Figure 2. Magnetic field maps and histograms during discharge (negative current) and charge (positive current) at different states of discharge (DOD) as indicated. The bottom right panel shows a simulation.

The battery leads in these measurements are located at the bottom of each map. The discharge capacity is indicative of the starting point of each step, and discharge measurements were performed before charge measurements. The imaging dimensions and the location of the cell (dotted rectangle) are indicated in the top left image.

Figure 3. Magnetic field maps and histograms as a function of overall discharge/charge current near full charge (DOD = 0 mAh). The imaging dimensions and the location of the cell (dotted rectangle) are indicated in the top left image.

Figure 4. (A) In the center, the spatially resolved map shows the result of a linear per-voxel fit of magnetic field vs. current, using all the current regimes measured (-125, -100, -75, -50, 50, 75, 100, 125mA). Several points are extracted for illustration, showing the magnetic field vs. current at each location. (B) Root mean square deviation of the linear fits across the whole volume performed by using different data combinations as indicated.

Figure 5. Histograms calculated from the magnetic field maps during discharging and charging for a damaged cell at 62.5 mAh DOD (after subtracting a reference image in the resting state).